Nuclear Materials and Energy 42 (2025) 101865

Contents lists available at ScienceDirect

Nuclear Materials and Energy

journal homepage: www.elsevier.com/locate/nme

SOLPS-ITER simulations to study the impact of aspect ratio on edge fueling neutrals in tokamaks

Yi-Cheng Chuang [a,*], Saskia Mordijck [a], Richard Fitzpatrick [b], Richard Reksoatmodjo [c]

[a] William & Mary, 200 Stadium Dr, Williamsburg, VA 23185, USA
[b] Institute for Fusion Studies, University of Texas at Austin, Austin, TX 78712, USA
[c] Lawrence Livermore National Laboratory, Livermore, CA 4551, USA

ARTICLE INFO

Keywords:
Spherical tokamak
Plasma edge modeling
Neutral opaqueness

ABSTRACT

In this paper, we examine the role of the aspect ratio on the neutral penetration and poloidal distribution for fixed magnetic geometry and plasma profiles using SOLPS-ITER. We start from an H-mode discharge from MAST (Kirk et al., 2012), with its aspect ratio of 1.4. We shift the magnetic equilibrium and vessel in major radius to generate a new SOLPS-ITER simulation, doubling the aspect ratio to 2.8. The neutral density profile perpendicular to the magnetic flux surfaces is fitted by an exponential. We find that the opaqueness, defined as the ratio between the electron pedestal density width and the neutral penetration depth, is unaffected by changes in the aspect ratio. We observe an increase in the neutral density close to the X-point on the high field side (HFS) as the aspect ratio increases. This poloidal angle averaged 44 % increase for the aspect ratio 2.8 case compared to the MAST geometry on the lower HFS is linked to an increase in the poloidal surface-integrated particle fluxes (1/s) towards the inner divertor.

1. Introduction

The spherical tokamak (ST) is an attractive concept for a compact magnetic confinement approach to a fusion pilot plant [1]. The pedestal at the plasma edge plays an important role in reaching fusion-relevant plasma conditions. In an ST, it has been observed that the pedestal pressure width is wider than in a regular tokamak [2]. New recent theoretical simulations indicate that the impact of gyrokinetic instabilities such as Micro Tearing Modes, Tearing modes, and Kinetic Ballooning Modes expand the pedestal width for spherical tokamaks [3]. However, the pedestal pressure structure is a construct of both temperature and density, and the impact of ionization on the pedestal density structure is an active topic of research in conventional tokamaks [4–7]. The impact of aspect ratio on ionization and neutral density profiles has not yet been explored, but it could influence the design of a pilot plant with respect to fueling and the fuel cycle.

In current-day devices, ionization plays a dominant role in determining the pedestal density structure [8]. The aspect ratio will not affect the mean free path of the neutrals if all plasma parameters remain similar; however, the machine size to mean free path ratio is altered. In a simplified view, as machine size increases, the ability of neutrals to penetrate inside the separatrix reduces. We find that machine size scaling, as only a function of major radius, R, has little impact on the neutral's ability to penetrate inside the separatrix. Additionally, the parallel flux in the Scrape-Off Layer will be affected by machine size. We find that this has especially a pronounced effect on the local neutral density close to the X-point on the High Field Side (HFS), where the relative changes in machine coordinates are more pronounced than on the Low Field Side (LFS), and the neutrals are confined to a smaller volume.

The opaqueness of neutrals allows us to compare the ability of neutrals to penetrate inside the separatrix. It is analogous to light attenuation through an opaque medium and is a dimensionless number characterized by taking the ratio of the pedestal density width, Δn_e (in mm), to the penetration depth of the neutrals, λ_{n0} (in mm). The pedestal width is determined by a tanh fit to the electron density, and the neutral penetration depth is found by fitting an exponential to the neutral density profile. As the calculation of the opaqueness requires detailed information on the pedestal and the neutral density profiles either obtained through experimental measurements and/or plasma-edge modeling, a heuristic approximation of opaqueness was developed, which does not depend on these measured and/or modeled quantities. This heuristic opaqueness is not dimensionless ($1/m^2$) and is expressed by $n_e \times a$, where $n_e = (n_e^{PED} + n_e^{SEP})/2$ and a is the minor radius [7]. Recent results comparing the penetration and ionization of

* Corresponding author.
E-mail address: ychuang@wm.edu (Y. Chuang).

https://doi.org/10.1016/j.nme.2025.101865
Received 4 July 2024; Received in revised form 20 December 2024; Accepted 6 January 2025
Available online 12 January 2025

hydrogen and deuterium at various levels of opaqueness have shown good agreement with the heuristic model by matching the pedestal dimensionless parameters without mass dependence [6,8].

In conventional tokamaks at low opaqueness, the ionization plays an important role in determining the pedestal density structure. The penetration of neutrals can shift the pedestal density outwards [9]. It also affects the width of the pedestal density [6]. At low opaqueness, divertor closure changes substantially influence the poloidal distribution of the neutrals, which in turn affects the width of the electron density pedestal [10]. However, at high opaqueness in conventional tokamaks, the neutral density and ionization have a limited effect on the pedestal density structure [4]. Recent SOLPS-ITER modeling and experiments show that these poloidal asymmetries and changes to the pedestal density structure disappear at higher opaqueness [6–8].

As experimental measurements for neutral densities inside the separatrix are not readily available, we rely on the heuristic approximation to identify lower and higher opaqueness regimes. Because the heuristic model depends only on the minor radius, it does not encompass the influence of aspect ratio and, thus, machine size. To isolate the impact of aspect ratio, we use SOLPS-ITER [11] to model a MAST H-mode discharge [12] and match the midplane electron density and temperature profiles. Next, we shift the magnetic equilibrium and the vessel as a function of the major radius in multiple steps and create a new grid for the SOLPS-ITER simulations, see Section 2. By fitting the SOLPS-ITER simulations, we can extract the opaqueness $\eta = \Delta n_e/\lambda_{n0}$ as a function of aspect ratio, which is discussed in Section 3. We find that the aspect ratio has no impact on the neutral opaqueness, but a change in the aspect ratio does affect the poloidal neutral density distribution. As the aspect ratio increases from 1.4 to 2.8, an increase in the neutral density on the high field side (HFS) is observed; see Section 4. We observe that this increase results from an increase in the poloidal Scrape-Off Layer particle flux, which depends on R, the major radius.

2. SOLPS-ITER simulations varying aspect ratio

The baseline MAST type-I ELM H-mode plasma scenario (27205) in this paper is a lower single null plasma, with a plasma current of 600 kA, a toroidal field of 0.55 T, and a $q_{95} \sim 2.8$ during the H-mode phase which starts at 0.24 s. The line-averaged density is 4×10^{19} m^{-3} and 3.6 MW of neutral beam injected (NBI) power is injected. The midplane profiles of the electron density and temperature are measured with the Thomson Scattering system and taken at 0.275 s.

We use the SOLPS-ITER code [11] to model this MAST experiment with the drifts turned off. The SOLPS-ITER code consists of two codes, $B2.5$, which solves the Braginskii plasma fluid equations, and $EIRENE$, a Monte-Carlo neutral code. Both are coupled and evolve until a steady-state solution is found. SOLPS-ITER requires user input for the cross-field transport, and the transport coefficients are determined by comparing and adjusting the SOLPS-ITER simulations until the simulations match the experimental measurements for the electron density, n_e, and temperature, T_e at the midplane, see Fig. 1. The transport coefficients are identical for all simulations; see Fig. 2. In addition, the core boundary conditions are set to a fixed density and temperature. The boundaries at the edge of the B2.5 SOL grid and Private Flux Region (PFR) are determined by flux leakage conditions. The particle flux leakage, $\Gamma_{loss} = \alpha_n C_{(s,e)} n_e$ approximates the radial loss as an advective flux based on the sound speed $C_{(s,e)}$, which is scaled by a parameter α_n, which is set to 10^{-3} in all our simulations. The electron heat flux leakage is similar $\Gamma_{loss} = \alpha_e C_{(s,e)} n_e T_e$ and in this case, α_e is set to 10^{-2} in all simulations. The EIRENE simulation initializes 9×10^5 particles and the boundary conditions are set to be fully recycling, except at the divertor plates, where the recycling is set at 0.99.

After determining the boundary conditions and transport coefficients based on the MAST experimental data, we shift the magnetic geometry and the vessel in major radius to regenerate a grid for SOLPS-ITER, see Fig. 3. The magnetic geometry is shifted along with the vessel

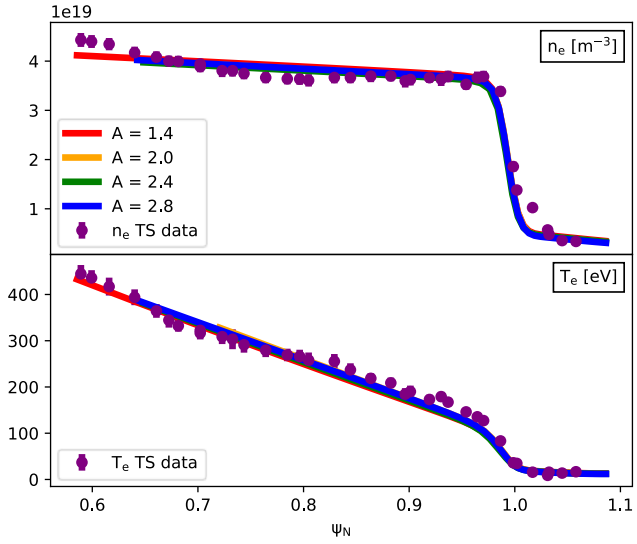

Fig. 1. (a) Electron density and (b) temperature mid-plane profile for discharge 27205 at 0.275 s. The purple circles and error bars are from the MAST Thomson Scattering system. The lines are the SOLPS-ITER simulations for the various aspect ratios starting at 1.4 (MAST, red), 2.0 (orange), 2.4 (green), and 2.8 (blue).

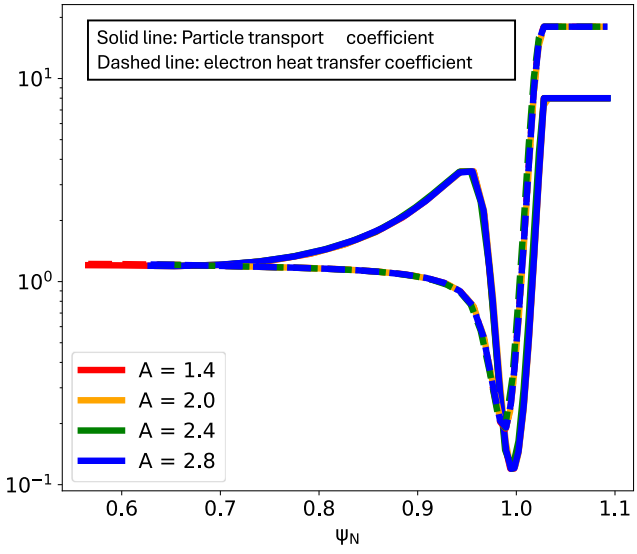

Fig. 2. Particle transport coefficient (solid line) and electron heat transport coefficient (dashed line) for SOLPS-ITER simulation. The lines' color labels are the same as Fig. 1.

structure, providing four different aspect ratios: 1.4, 2.0, 2.4, and 2.8. In comparison, DIII-D has an aspect ratio of 2.5, and C-Mod and ITER have an aspect ratio of 3.1. With the same boundary conditions and perpendicular transport coefficients, all the simulations have identical electron density and temperature profiles at the midplane; see Fig. 1. The location of the inner grid boundary depends on the grid reconstruction. Still, it is always far enough from the separatrix to allow us to study the impact on the neutral density.

3. Neutral opaqueness

Opaqueness is defined as the ratio of the electron pedestal density width and the neutral penetration length, $\eta = \Delta n_e/\lambda_{n0}$. It is a dimensionless number that allows for the comparison between different devices and experimental scenarios. It is a poloidally and toroidally localized value, which can vary due to magnetic flux expansion.

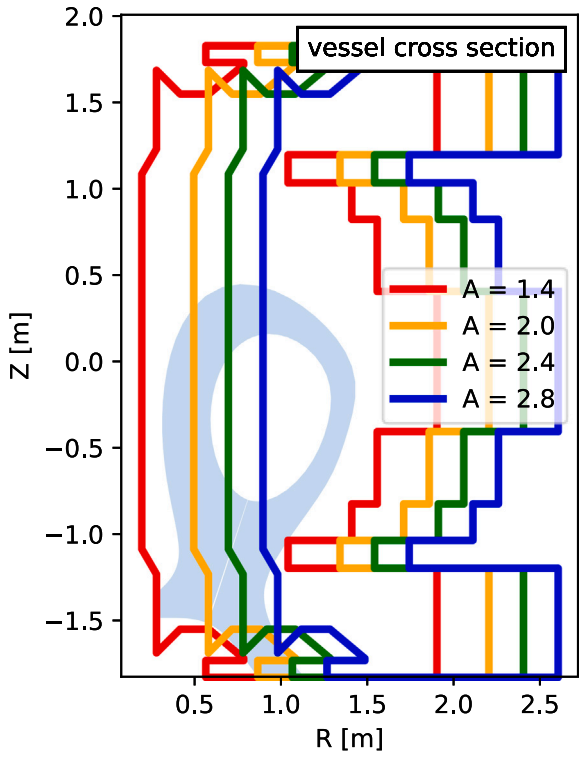

Fig. 3. Vessel cross-section and magnetic configuration for the SOLPS-ITER simulations for MAST (red). The additional vessel geometries correspond to the shifts in radius and thus aspect ratio at 2.0 (orange), 2.4 (green), and 2.8 (blue).

To extract the electron density pedestal width, Δn_e, we fit a tanh to the SOLPS-ITER modeled electron density profiles [4]. The tanh fit is applied at each poloidal angle of the SOLPS-ITER simulation and mapped from flux space to machine coordinates for each poloidal location. The resulting Δn_e as a function of poloidal angle is shown in Fig. 4(a). The pedestal width is constant in flux space, as the electron quantities are constant on a flux surface, but due to flux expansion, the pedestal width is not constant in machine coordinates. The Grad–Shafranov shift means that the width is narrower on the LFS and wider on the HFS by about a factor 2 [13], see Fig. 4. The width increases substantially close to the X-point, which leads to a pronounced flux expansion due to magnetic geometry flux. As all simulations have similar pedestal density profiles, there is thus no change in pedestal width as a function of aspect ratio.

To extract the neutral penetration depth, λ_{n0}, we fit an exponential to the neutral density calculated by SOLPS-ITER at each poloidal location [14], see Fig. 5.

$$n_0 = n_0^{pb} e^{(\Psi_N^{pb} - \Psi_N)/\lambda_{n0}} \tag{1}$$

n_0 is the atomic neutral density, n_0^{pb} and Ψ_N^{pb} are the atomic neutral density and Ψ_N value at the foot of pedestal density, and $\lambda_{n0}(\Psi_N)$ is the neutral penetration depth as function of Ψ_N. The fit is limited to the neutral density profile that spans the electron density pedestal width. In the second step, $\lambda_{n0}(\Psi_N)$ is transformed to machine coordinates, with the units of mm, at each poloidal location to incorporate information on flux expansion. The neutral penetration depth λ_{n0} is wider than the pedestal width, which has been observed in DIII-D experimentally at low opaqueness [6], especially on the LFS, see Fig. 4. The neutral penetration depth, λ_{n0}, also increases on the HFS similar to the pedestal width, but only by a factor of 1.5, and again, a large increase is observed close to the lower X-point. No substantial variation is observed between the different aspect ratios, which suggests that with respect

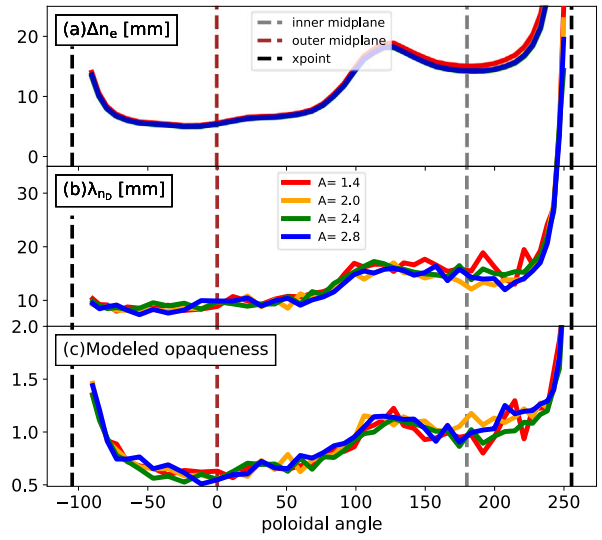

Fig. 4. (a) Electron density pedestal width, Δn_e, (b) neutral penetration length, λ_{n0}, and (c) opaqueness, η, versus poloidal angle for various aspect ratios starting at 1.4 (MAST, red), 2.0 (orange), 2.4 (green), 2.8 (blue). The dashed black vertical lines indicate the location of the lower X-point in the simulation. The brown dashed line is the outer midplane, and the gray dashed line is the inner midplane.

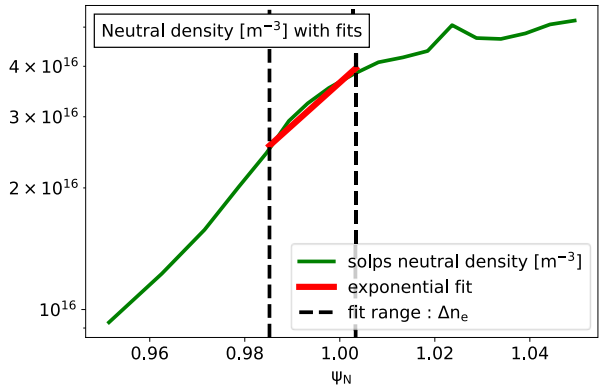

Fig. 5. SOLPS-ITER calculated neutral density profile at the midplane (green). The dashed black lines indicate the density pedestal width and its location. The exponential fit to the profile for the pedestal width region is shown in red.

to neutral dynamics when plasma conditions are identical, the aspect ratio has little influence on neutral dynamics inside the separatrix.

With both the pedestal density width and the neutral penetration depth, we can now calculate the opaqueness, $\eta = \Delta n_e / \lambda_{n0}$, see Fig. 4(c). The opaqueness is close to 1 as a function of the poloidal angle for all aspect ratios. On the LFS, the opaqueness is just below 1, and on the HFS, the opaqueness increases above 1. The results are susceptible to small variations in either electron density width as a function of flux expansion, which is best illustrated at the X-point. Counter to intuition, we observe an increase in opaqueness, while it is often assumed that X-point fueling dominates [15]. As observed in earlier simulations, the neutral density close to the X-point is higher in low opaqueness plasmas [8,14].

The overall observation is that the opaqueness is unaffected by changes in aspect ratio while keeping all other parameters constant. In reality, the pedestal density width will not be a constant function of the aspect ratio, directly affecting the opaqueness calculation. One assumption is that as the aspect ratio decreases, the density pedestal width increases due to changes in transport and stability [3]. If we assume similar scaling as observed and modeled for the pedestal pressure

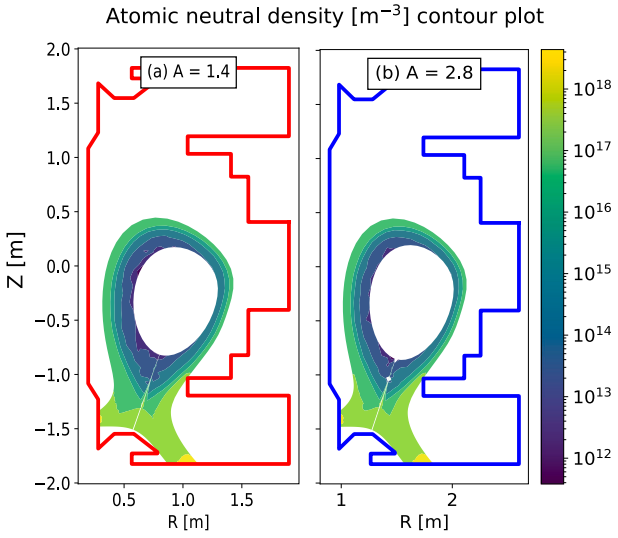

Fig. 6. Atomic neutral density contour plot calculated with SOLPS-ITER for aspect ratio (a) 1.4 (left, MAST) and (b) 2.8 (right).

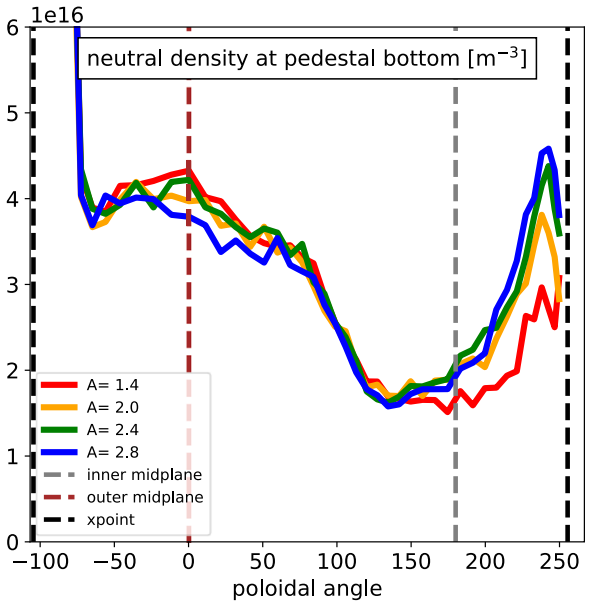

Fig. 7. Fitted atomic neutral density at the separatrix versus poloidal angle. The lines are the SOLPS-ITER simulations for the various aspect ratios starting at 1.4 (MAST, red), 2.0 (orange), 2.4 (green), and 2.8 (blue). The dashed black vertical lines indicate the location of the lower X-point in the simulation. The brown and gray dashed lines are the outer and inner midplane.

width [2,3], this will result in an increase in opaqueness for a reduced aspect ratio. A secondary effect is that as the electron density pedestal profile increases in width, this will affect the neutral penetration as well. A simple example of the influence of the pedestal width (in machine coordinates) can be seen in Fig. 4, which looks at the influence of flux expansion. While the pedestal width increases by a factor of 2 between LFS and HFS, the neutral penetration only increases by 1.5. This would suggest that while spherical tokamaks are more compact, their opaqueness could be higher than that of conventional tokamaks for similar electron densities due to the widening of the pedestal.

4. Poloidal variation of neutral density

While the penetration depth might not vary inside the separatrix, this does not mean that the neutral density was not affected by changes in aspect ratio. Fig. 6 shows the 2D neutral density profiles calculated by SOLPS-ITER for the original MAST case and the case with the large shift in R and an aspect ratio of 2.8. Light colors represent higher neutral densities, while dark colors represent lower neutral densities. The neutral densities on the HFS are higher for the shifted case than for the original MAST case.

To identify systemic changes in the neutral density as a function of aspect ratio, we investigate the neutral density at the pedestal bottom as a function of the poloidal angle. The neutral density at the pedestal bottom, n_0^{pb}, is calculated by Eq. (1) instead of using the direct values from the EIRENE simulation. The use of the fit 'smooths' the noisy variation in neutral density values that occurs due to Monte-Carlo noise and improves the ability for comparison. Fig. 7 shows the separatrix neutral densities as a function of the poloidal angle, with the LFS midplane at 0 degrees and the HFS midplane at 180. The dark dashed lines are the X-point locations. The neutral density at the separatrix does not vary substantially on the LFS, but there is a substantial increase as a function of increasing aspect ratio on the HFS. For the original MAST case, the neutral density from the HFS midplane up till the X-point is much lower. The most significant increase is from aspect ratio 1.4 (red) to 2.0 (yellow), but the neutral density keeps increasing with increasing aspect ratio, see Fig. 7.

The atomic neutral density increase with aspect ratio can be linked to increased parallel surface-integrated particle fluxes (1/s) to the divertor. The continuity equation in *B*2.5 [16] is expressed as:

$$\frac{\partial n}{\partial t} + \frac{1}{\sqrt{g}}\frac{\partial}{\partial \theta}\left(\frac{\sqrt{g}}{h_\theta}\Gamma_\theta\right) + \frac{1}{\sqrt{g}}\frac{\partial}{\partial r}\left(\frac{\sqrt{g}}{h_r}\Gamma_r\right) = S_n \qquad (2)$$

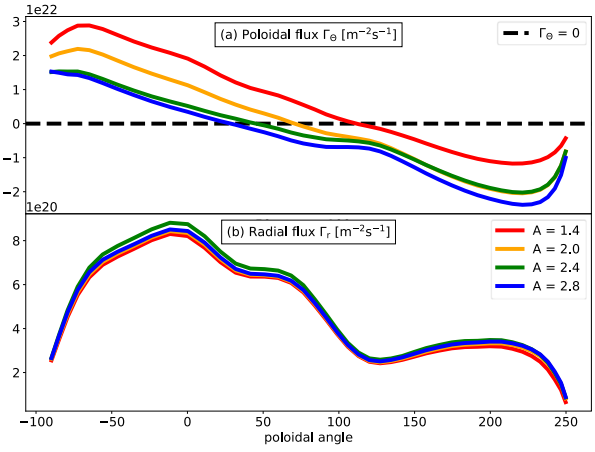

Fig. 8. Poloidal plot for (a) poloidal and (b) radial flux at the separatrix. The positive poloidal flux direction is towards the outer target, and the positive radial flux direction is towards the wall. The black dashed line shows the poloidal flux stagnation point for each simulation case. The data lines' color labels are the same as Fig. 7.

Where r stands for the radial and θ for the poloidal angle direction on the curvilinear *B*2.5 grid. In this equation, n is the plasma density, S_n is the source from the neutrals, and $\Gamma_{r,\theta}$ is the radial and poloidal particle fluxes in the *B*2.5 grid. To map these particle fluxes from the computation domain Cartesian grid (Ψ_N space) to the 2D curvilinear grid (real space), *B*2.5 uses geometry coefficients in radial, h_r, poloidal, h_θ, and toroidal, h_ϕ direction. The coordinate transform Jacobian $\sqrt{g} = h_r h_\theta h_\phi$. Here $h_\phi = 2\pi R$, and $h_{r,\theta} = 1/\|\nabla r, \theta\|$.

The radial flux in the simulations shows no change as a function of the shift in R, see Fig. 8(b); however, the poloidal flux shifts 'downward' as a function of the increase in R. This means that the 'stagnation' point where the flow could go in either direction moves from the crown of the plasma for a MAST aspect ratio to the outer

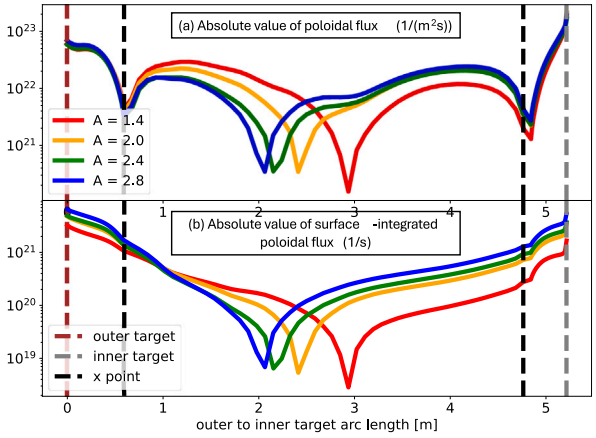

Fig. 9. Absolute value of (a) poloidal flux ($1/(m^2s)$), and (b) surface-integrated poloidal flux ($1/s$) versus outer to inner target separatrix arc length. The brown and gray dashed lines are the outer and inner target locations. The black dashed line is the lower X-point location. The data lines' color labels are the same as Fig. 7.

midplane as the aspect ratio increases, see Fig. 8(a). The change in poloidal flux is most pronounced in the initial increase in aspect ratio but saturates at the most significant aspect ratios modeled in this paper.

The poloidal fluxes, Γ_θ $(1/(m^2s))$, at the targets are the same for all cases because the sheath boundary condition and the upstream electron density and temperature are the same for all aspect ratios; see Fig. 9(a). The cusp in each simulation case is the saturation point. Because of the fixed density boundary condition, the input surface-integrated poloidal flux, $(\sqrt{g}/h_\theta)\Gamma_\theta$ $(1/s)$, at the core increases with major radius R. Therefore, the surface-integrated poloidal flux at the separatrix increases with the aspect ratio; see Fig. 9(b). This increase in surface-integrated poloidal flux to the divertors means that more particles will be recycled in this region, as the recycling coefficient is fixed in these simulations. The number of neutrals increases in the divertors as the simulations all reach a steady state with $\partial n/\partial t \approx 0$. The higher neutral density content in the inner divertor region shows up as an increase in neutral density at the separatrix close to the X-point on the HFS. However, the increase in neutrals is not significant enough in these simulations to drastically change the inner divertor conditions, such as going from attached to detached conditions. Although the surface-integrated poloidal flux at the outer target increases with the aspect ratio, neutral density on the LFS decreases with the aspect ratio due to the saturation point shift.

The atomic neutral density changes on the LFS are less pronounced. This is linked to multiple factors, such as the previously mentioned saturation point shift, ionization source term change, chamber volume, and neutral baffle. The primary source term at the separatrix is ionization. The atomic neutral density is proportional to the ionization term, S_{ion}, in our identical electron density and temperature setting with the formula: $S_{ion} = n_e n_0 \langle \sigma_{ion} v_e \rangle$, where $\langle \sigma_{ion} v_e \rangle$ is ionization rate. We define Δ as the operator for the quantity difference between two aspect ratio cases, A_1 and A_2. The source term difference, ΔS,equals to the particle flux divergence difference, $\Delta(\nabla \cdot \Gamma)$, because of the steady state continuity equation, i.e.,

$$\begin{aligned}\Delta S &= \Delta(\nabla \cdot \Gamma) \\ &= \Delta\left(\frac{1}{R}\left[\frac{1}{2\pi h_r h_\theta}\frac{\partial}{\partial\theta}\left(\frac{\sqrt{g}}{h_\theta}\Gamma_\theta\right)\right.\right. \\ &\left.\left. + \frac{1}{2\pi h_r h_\theta}\frac{\partial}{\partial r}\left(\frac{\sqrt{g}}{h_r}\Gamma_r\right)\right]\right) \end{aligned} \tag{3}$$

If the term inside the square bracket in Eq. (3), $R\nabla\cdot\Gamma$, and its difference, $\Delta(R\nabla \cdot \Gamma)$, are compatible on both sides, the major radius reciprocal difference, $\Delta(1/R)$, dominates. Based on the following equation,

$$\begin{aligned}\frac{1}{R_{HFS_1}} - \frac{1}{R_{HFS_2}} &= \frac{\Delta R}{R_{HFS_1} R_{HFS_2}} \\ > \frac{\Delta R}{R_{LFS_1} R_{LFS_2}} &= \frac{1}{R_{LFS_1}} - \frac{1}{R_{LFS_2}},\end{aligned} \tag{4}$$

the change in the ionization source term is smaller on the LFS, where R_{HFS_1}, R_{HFS_2}, R_{LFS_1}, R_{HFS_2} are the local major radius on the HFS and LFS for two aspect ratio cases, A_1 and A_2. Moreover, the neutrals have a larger volume in which they can interact with the LFS, thus limiting the impact on the neutral density close to the separatrix. The baffle structure on the LFS close to the X-point, as shown in Figs. 3 and 6, also blocks the atomic neutrals from diffusing to the upper LFS, as shown in atomic neutrals density plummet at around poloidal angle −75° in Fig. 7.

5. Discussion and conclusion

In this paper, we investigate the role of aspect ratio on the opaqueness and the neutral density using SOLPS-ITER simulations. We shift the magnetic equilibrium and vessel in 4 simulations from 1.4 to 2.8 aspect ratio. Each simulation has the same transport coefficients and boundary conditions, leading to similar plasma profiles. We find that the change in aspect ratio has no impact on the opaqueness of these plasma conditions. The opaqueness in these simulations is similar to previous results from DIII-D at low opaqueness on DIII-D [6]. The following steps would be to increase the opaqueness through an increase in the electron density and vary the temperature to alter the contributions of charge exchange to investigate whether aspect ratio in more fusion-relevant regimes would play a role. In addition, a scan of the pedestal electron density width can be performed to investigate the influence of these parameters on the opaqueness, as it also affects the neutral penetration depth.

The role of the aspect ratio on poloidal flows is not a result that can be tested experimentally. The stagnation point in normal aspect ratio tokamaks is close to the LFS midplane. The exact location depends on plasma conditions, drifts, and magnetic configuration. As most spherical tokamaks operate in a double null configuration, information on the stagnation point location and parallel flows specific to a spherical tokamak is not applicable to this single lower null simulation. The next steps would include testing the impact of magnetic geometry and drifts on these results.

The impact of the increase in parallel flows to the inner divertor at a normal aspect ratio and, thus, the creation of a higher neutral density region matches observations that a high neutral density front can form on the high field side in H-mode, as observed in both JET and AUG [17,18]. The lack of a natural higher neutral density on the lower high field side in a spherical tokamak could also be responsible for why they might be more sensitive to localized fueling in altering density profiles and even access to H-mode [19]. To test this further, additional SOLPS-ITER modeling should be performed on varying poloidal fueling locations and direct comparisons with new experiments that alter the poloidal fueling location and enhanced ionization measurements.

CRediT authorship contribution statement

Yi-Cheng Chuang: Writing – original draft, Visualization, Methodology, Investigation. **Saskia Mordijck:** Writing – review & editing, Supervision, Methodology, Conceptualization. **Richard Fitzpatrick:** Conceptualization. **Richard Reksoatmodjo:** Software.

Declaration of competing interest

The authors declare that they have no known competing financial interests or personal relationships that could have appeared to influence the work reported in this paper.

Acknowledgments

This material is based upon work supported by the U.S. Department of Energy, Office of Science, Office of Fusion Energy Sciences DE-SC0021306, DE-SC0007880, DE-SC0023372, DE-SC0021156.

The authors acknowledge William & Mary Research Computing for providing computational resources and technical support that have contributed to the results reported within this paper. https://www.wm.edu/it/rc

Y. Chuang thanks E. Emdee and M. Miller for the helpful advice on running SOLPS-ITER. The input transport coefficient is generated using the SOLPSxport code [20].

Data availability

The authors do not have permission to share data.

References

[1] A. Costley, Towards a compact spherical tokamak fusion pilot plant, Phil. Trans. R. Soc. A 377 (2141) (2019) 20170439.

[2] A. Diallo, J. Canik, T. Göerler, S.-H. Ku, G. Kramer, T. Osborne, P. Snyder, D. Smith, W. Guttenfelder, R. Bell, D. Boyle, C.-S. Chang, B. LeBlanc, R. Maingi, M. Podestà, S. Sabbagh, Progress in characterization of the pedestal stability and turbulence during the edge-localized-mode cycle on National Spherical Torus Experiment, Nucl. Fusion 53 (9) (2013) 093026.

[3] J. Parisi, W. Guttenfelder, A.O. Nelson, R. Gaur, A. Kleiner, M. Lampert, G. Avdeeva, J.W. Berkery, C. Clauser, M. Curie, et al., Kinetic-ballooning-limited pedestals in spherical tokamak plasmas, Nucl. Fusion (2023).

[4] J.W. Hughes, B. LaBombard, A.D. Mossessian, A.E. Hubbard, J. Terry, T. Biewer, the Alcator C-Mod Team, Advances in measurement and modeling of the high-confinement-mode pedestal on the Alcator C-Mod tokamak, Phys. Plasmas 13 (5) (2006) 056103.

[5] A.M. Rosenthal, J.W. Hughes, F.M. Laggner, T. Odstrčil, A. Bortolon, T.M. Wilks, F. Sciortino, Inference of main ion particle transport coefficients with experimentally constrained neutral ionization during edge localized mode recovery on DIII-D, Nucl. Fusion 63 (4) (2023) 042002.

[6] R. Chaban, S. Mordijck, A.M. Rosenthal, M. Knolker, F.M. Laggner, T.H. Osborne, L. Schmitz, K.E. Thome, T.M. Wilks, The role of isotope mass on neutral fueling and density pedestal structure in the DIII-D tokamak, Nucl. Fusion 64 (2024) 046008.

[7] S. Mordijck, Overview of density pedestal structure: role of fueling versus transport, Nucl. Fusion 60 (8) (2020) 082006, http://dx.doi.org/10.1088/1741-4326/ab8d04.

[8] S. Mordijck, R. Chaban, R. Reksoatmodjo, J.B. Arias, Y. Chuang, J. Loughran, J.W. Hughes, A.M. Rosenthal, M. Miller, T. Wilks, F. Laggner, T. Osborne, Impact of ionization and transport on pedestal density structure in DIII-D and Alcator C-Mod, Nucl. Fusion (2024).

[9] M.G. Dunne, S. Potzel, F. Reimold, M. Wischmeier, E. Wolfrum, L. Frassinetti, M. Beurskens, P. Bilkova, M. Cavedon, R. Fischer, B. Kurzan, F.M. Laggner, R.M. McDermott, G. Tardini, E. Trier, E. Viezzer, M. Willensdorfer, T. EUROfusion MST1 Team, The ASDEX Upgrade Team, The role of the density profile in the ASDEX Upgrade pedestal structure, Plasma Phys. Control. Fusion 59 (1) (2016) 014017, http://dx.doi.org/10.1088/0741-3335/59/1/014017.

[10] A.L. Moser, L. Casali, B.M. Covele, A.W. Leonard, A.G. McLean, M.W. Shafer, H.Q. Wang, J.G. Watkins, Separating divertor closure effects on divertor detachment and pedestal shape in DIII-D, Phys. Plasmas 27 (3) (2020).

[11] X. Bonnin, W. Dekeyser, R. Pitts, D. Coster, S. Voskoboynikov, S. Wiesen, Presentation of the new SOLPS-ITER code package for tokamak plasma edge modelling, Plasma Fusion Res. 11 (2016) 1403102, http://dx.doi.org/10.1585/pfr.11.1403102.

[12] A. Kirk, I.T. Chapman, J. Harrison, Y. Liu, E. Nardon, S. Saarelma, R. Scannell, A.J. Thornton, et al., Effect of resonant magnetic perturbations with toroidal mode numbers of 4 and 6 on edge-localized modes in single null H-mode plasmas in MAST, Plasma Phys. Control. Fusion 55 (1) (2012) 015006.

[13] H. Zohm, Magnetohydrodynamic Stability of Tokamaks, John Wiley & Sons, 2015.

[14] R. Reksoatmodjo, S. Mordijck, J. Hughes, J. Lore, X. Bonnin, The role of edge fueling in determining the pedestal density in high neutral opacity Alcator C-Mod experiments, Nucl. Mater. Energy (ISSN: 2352-1791) 27 (2021) 100971, http://dx.doi.org/10.1016/j.nme.2021.100971.

[15] M. Groth, L.W. Owen, G.D. Porter, N.H. Brooks, M.E. Fenstermacher, W.H. Meyer, A.W. Leonard, T.W. Petrie, D.L. Rudakov, G. Wang, et al., Assessment of the poloidal distribution of core plasma fueling and impurity sources in DIII-D, J. Nucl. Mater. 337 (2005) 425–430.

[16] W. Dekeyser, Optimal Plasma Edge Configurations for Next-Step Fusion Reactors (Ph.D. thesis), KU Leuven, 2014.

[17] S. Potzel, M. Wischmeier, M. Bernert, R. Dux, F. Reimold, A. Scarabosio, S. Brezinsek, M. Clever, A. Huber, A. Meigs, et al., Formation of the high density front in the inner far SOL at ASDEX Upgrade and JET, J. Nucl. Mater. 463 (2015) 541–545.

[18] F. Reimold, M. Wischmeier, S. Potzel, L. Guimarais, D. Reiter, M. Bernert, M. Dunne, T. Lunt, A. Team, et al., The high field side high density region in SOLPS-modeling of nitrogen-seeded H-modes in ASDEX Upgrade, Nucl. Mater. Energy 12 (2017) 193–199.

[19] A.R. Field, P.G. Carolan, N.J. Conway, G.F. Counsell, G. Cunningham, P. Helander, H. Meyer, D. Taylor, M.R. Tournianski, M.J. Walsh, et al., The influence of gas fuelling location on H-mode access in the MAST spherical tokamak, Plasma Phys. Control. Fusion 46 (6) (2004) 981.

[20] R. Wilcox, J. Lore, SOLPSxport, URL https://github.com/ORNL-Fusion/SOLPSxport.